

A 2D MoS₂-Based Active-Matrix Photosensor Array for Neuromorphic Vision

Yitong Chen, Rui Wang, Siyu Zhang, Feilin Chen, Yingjie Tang, Shuhui Ren, Dingwei Li, Yan Wang, Huihui Ren, Guolei Liu, Fanfan Li, Hong Wang,* and Bowen Zhu*

Neuromorphic visual processing hardware mimics key functions of the human visual system, including static image sensing and processing, as well as the perception and prediction of moving targets. However, conventional complementary metal-oxide semiconductor (CMOS) platforms face significant challenges such as power consumption and processing delays. Herein, a 64 × 64 active-matrix photosensor array (AM-PA) is developed with a one-transistor-one-photodetector architecture, by integrating metal-oxide thin-film transistors with monolayer MoS₂ photodetectors. By modulating the intrinsic defects serving as charge-trapping centers within the MoS₂ film, the AM-PA exhibits configurable conductance plasticity in response to optical stimuli. This system enables in-array visual sensing and processing functionalities: static image sensing and pre-processing to reduce noise, prediction of dynamic spatiotemporal patterns, and accurate trajectory forecasting for complex motion scenarios. These results demonstrate the feasibility of the AM-PA as a promising platform for neuromorphic visual systems.

1. Introduction

Vision is the primary sensory modality of humans in interpreting their surroundings, and humans perceive visual information

Y. Chen, H. Ren
School of Materials Science and Engineering
Zhejiang University
Hangzhou 310027, China
Y. Chen, S. Zhang, F. Chen, Y. Tang, S. Ren, D. Li, Y. Wang, H. Ren, G. Liu,
F. Li, B. Zhu
Zhejiang Key Laboratory of 3D Micro/Nano Fabrication and
Characterization
School of Engineering
Westlake University
Hangzhou, Zhejiang 310030, China
E-mail: zhubowen@westlake.edu.cn
R. Wang, H. Wang
Key Laboratory of Wide Band Gap Semiconductor Technology
School of Microelectronics Xidian University
Xi'an 710071, China
E-mail: hongwang@xidian.edu.cn
B. Zhu
Westlake Institute for Optoelectronics
Hangzhou 311421, China

The ORCID identification number(s) for the author(s) of this article can be found under <https://doi.org/10.1002/adfm.202507954>

DOI: 10.1002/adfm.202507954

in an intelligent and efficient way. In comparison, conventional complementary metal-oxide semiconductor (CMOS) cameras face limitations in color perception due to the use of splitting prisms and challenges in color reconstruction.^[1–4] They are also restricted to spatial frame acquisition without temporal data integration, while attempts at temporal fusion imaging require high power due to extensive signal transmission requirements.^[5–6] Recently, emerging neuromorphic visual hardware emulates the human visual system by implementing in-sensor processing functions, such as noise suppression, feature extraction, and motion prediction.^[7–11] This approach minimizes data redundancy, conserves power, and enables more efficient tasks, including object detection, color perception, and motion sensing.^[12–17]

Neuromorphic visual hardware has thus garnered significant interest, driven by retina-inspired strategies that integrate functional materials, ranging from metal oxides to two-dimensional (2D) materials and their heterostructures, realizing simultaneous sensing and processing of both static images and dynamic senses.^[18–27] In particular, 2D materials like transition metal dichalcogenides (TMDs) stand out for their strong light absorption and high sensitivity at the atomic scale, enhancing the resolution and performance of artificial visual systems.^[28–34] Despite these advantages, existing 2D-based sensor configurations are often restricted to discrete devices or small passive arrays, resulting in low spatial resolution, increased signal crosstalk, and slower response times, collectively hindering real-time in-sensor processing of complex motions and dynamic imaging tasks.^[35–43] Therefore, integrating 2D materials with active-matrix architectures is crucial to fully exploit the benefits of precisely localized signal control, scalable pixel arrays, and dynamic data processing. Such integration enables real-time adaptation to changing inputs, more efficient spatial-temporal data fusion, and advanced neuromorphic functions such as predictive motion tracking within the sensor array.

Herein, we report a 64 × 64 active-matrix photosensor array (AM-PA) that integrates lanthanide-doped indium zinc oxide (Ln-IZO) thin-film transistors (TFTs) as switching elements with monolayer MoS₂ photodetectors. The MoS₂ layer features intrinsic defects that act as charge-trapping centers, enabling light information storage and dynamic modulation of the device's

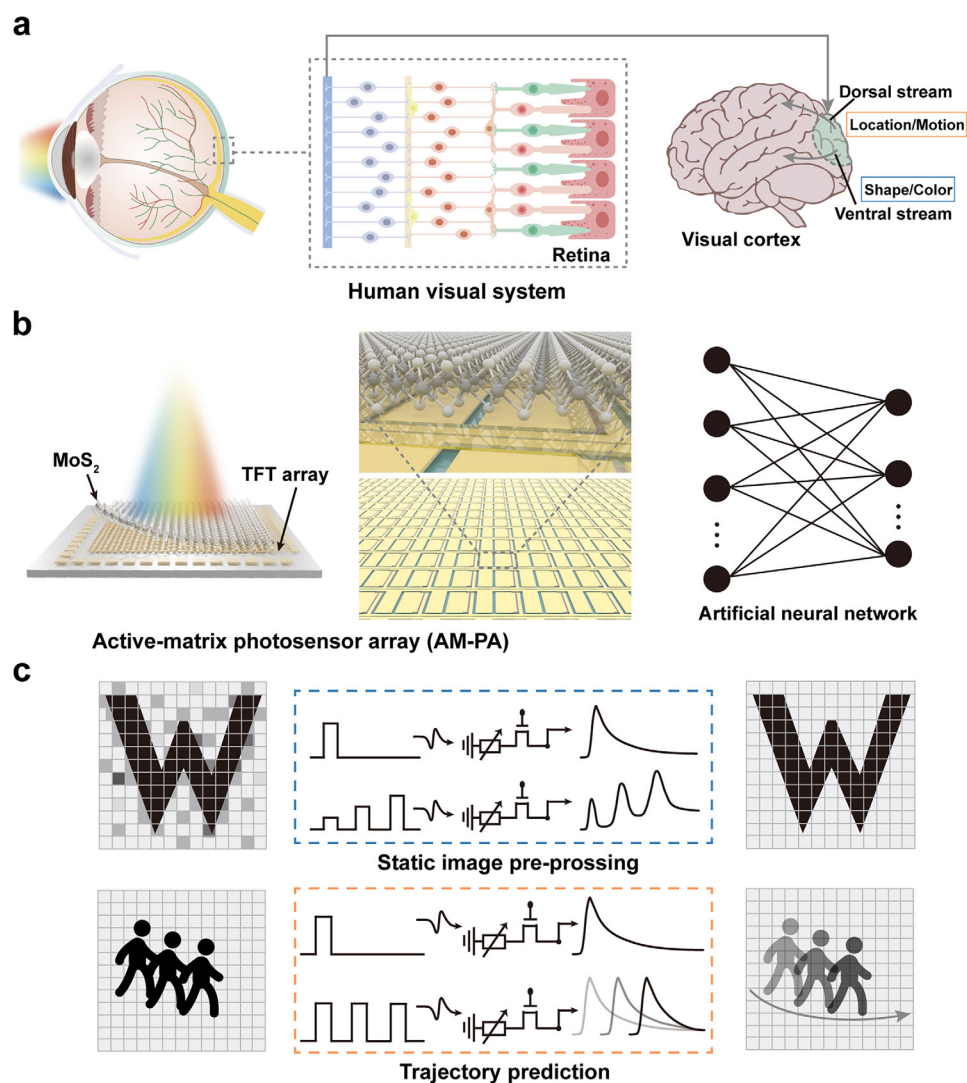


Figure 1. Neuromorphic visual processing hardware is inspired by the human visual system. a) Schematic diagram of the human visual system. The human visual system is a complex network combining optical components for focusing light and neural systems (retina and visual cortex) for processing and interpreting visual information, enabling perception of object shape, color recognition, spatial location, and motion processing. b) Schematic illustration of the neuromorphic visual processing hardware. This system emulates the human visual system using an active-matrix photosensor array (AM-PA) with a 64×64 -pixel array of lanthanide-doped indium zinc oxide (Ln-IZO) thin-film transistors (TFTs) and a monolayer 2D molybdenum disulfide (MoS₂) photodetector (PD). c) Schematic illustration of the AM-PA for static image pre-processing and trajectory prediction.

optoelectronic properties, capable of short-term memory (STM), long-term memory (LTM), and color-sensitive functionalities. Leveraging its light-tunable conductance, the AM-PA operates as a neuromorphic visual hardware, enabling static image sensing and effective noise reduction through in-sensor pre-processing. Furthermore, its spatiotemporal processing capabilities were experimentally validated, achieving high image fidelity with a Structural Similarity Index Measure (SSIM) value of 0.95 while predicting dynamic visual inputs and accurately forecasting advanced motion trajectories with 92% accuracy. This demonstration of an active-matrix sensor array with optically configurable capabilities shows considerable promise for neuromorphic visual processing systems.

2. Results

2.1. Design of the Active-Matrix Photosensor Array (AM-PA) Inspired by Human Vision

In the human visual system, the retina and visual cortex play central roles in the perception of sight (**Figure 1a**). This system enables the perception of light, color, shape, and depth through an intricate network encompassing the eyes, optical pathways, and brain. Light enters the eye via the cornea and pupil, where it is focused by the lens onto the retina. The retina, which contains photoreceptors (rods for low-light conditions and cones for color vision), converts light into electrical signals. These signals

travel through the optic nerve to the brain, reaching the primary visual cortex in the occipital lobe, where fundamental visual features, such as edges and orientations, are initially processed. Subsequently, visual information is conveyed through the ventral pathway (“what” pathway) for object shape and color recognition and the dorsal pathway (“where/how” pathway) for spatial location and motion processing. This interconnected system enables complex visual perception, essential for object recognition, scene interpretation, and effective interaction with the environment.

Inspired by the human visual system, we designed an active-matrix photosensor array (AM-PA) that mimics its functionality, incorporating a 64×64 -pixel array of lanthanide-doped indium zinc oxide (Ln-IZO) thin-film transistors (TFTs) and a monolayer 2D molybdenum disulfide (MoS_2) photodetector (PD) (Figure 1b). The monolayer MoS_2 PD functions as photoreceptors, converting red/green/blue lights into electrical signals, and exhibiting light configurable conductance characteristics. Meanwhile, the Ln-IZO TFT array functions as an active switch, selectively routing the PD’s photocurrent to the readout circuitry. When the TFT is off, the current of the MoS_2 PD remains isolated, keeping the pixel current at a low level and reducing crosstalk. Conversely, turning the TFT on creates a conductive channel that directs the PD’s output to the source terminal and then to the data line. By controlling the gate voltage, each pixel’s PD signal is isolated or shared with the data line at precise intervals. This arrangement enables robust, low-power operation, minimal crosstalk, and temporal integration of the photocurrent.^[44,45] Leveraging the light-dependent photosensitive effect and the time-resolved response of historical inputs, the AM-PA operates with integrated functions of sensing, memory, and contrast enhancement, facilitating the pre-processing of static images (Figure 1c). Additionally, this functionality enables dynamic scene analysis, allowing the prediction of moving objects’ trajectories with high accuracy (Figure 1d).

2.2. Electrical Characteristics of the Thin-Film Transistors (TFTs) in AM-PA

The AM-PA comprises a 64×64 -pixel array of monolayer MoS_2 PDs for light sensing, integrated with an active-matrix backplane featuring Ln-IZO TFTs for switching and data addressing. The schematic diagram of a single pixel within the AM-PA is shown in Figure 2a. The fabrication process and structural details are outlined in the Experimental Section and Figure S1 (Supporting Information). Once the TFT backplane is fabricated, a passivation layer is deposited to support the integration of the PD on top. This layer also serves as an interface dielectric and was selectively patterned to expose the electrode areas. As a result, when the MoS_2 layer was transferred onto the backplane, it only formed electrical contact at the exposed electrode regions, establishing electrical connections between the backplane and PDs. The cross-sectional transmission electron microscopy (TEM) images and the corresponding elemental distribution are presented in Figure S2 (Supporting Information), revealing the layered composition and confirming the proper integration of the MoS_2 layer. Figure 2b presents the fully assembled backplane and the magnified optical microscope images of individual pixels, demonstrating the structural integrity and uniformity. The backplane utilizes TFT

technology initially developed for high-resolution displays and was utilized to manufacture the backplane designed for the photosensor array. To optimize the functionality, the switch Ln-IZO TFTs occupy a smaller area than the MoS_2 PD, ensuring effective light sensing and precise readout control. The array achieves a resolution of 163 ppi, covering a $1 \times 1 \text{ cm}^2$ area. A detailed performance comparison with the optoelectronic device array is shown in Table S1 (Supporting Information). Each pixel in AM-PA follows a 1T-1PD architecture, as depicted in the equivalent circuit diagram in Figure 2c. The scan line applies voltage (V_{SL}) to the switch TFT gate, while the data line delivers the readout voltage (V_{DL}).

Upon illumination, the MoS_2 PD generates a photocurrent through electron-hole pair generation, with photogenerated electrons trapped in localized states inducing persistent photoconductivity, as will be discussed later. An important advantage of this integrated architecture is the elimination of a dedicated storage capacitor for the sensing part, as the persistent photoconductivity of the MoS_2 PD inherently retains the photogenerated signal.^[44,45] This design reduces pixel complexity, enabling higher-resolution arrays, simplified fabrication, and lower power consumption, making it highly suitable for advanced optoelectronic applications. Figure 2d presents the transfer curves of Ln-IZO TFT before and after integration with the MoS_2 PD, measured with a gate voltage (V_{GS}) sweep from -10 to 20 V and a constant drain voltage (V_{DS}) of 10 V , demonstrating stable switching performance. When the switch TFT is off, the photodetector current remains isolated, reducing pixel current to as low as ten pA and effectively preventing crosstalk. When the switch TFT is turned on and V_{DL} is applied, the photodetector current becomes accessible for measurement. Additionally, we have conducted measurements of the transfer characteristics of Ln-IZO TFT, under both negative/positive bias stress (NBS/PBS) and negative/positive bias illumination stress (NBIS/PBIS) (Figure S3, Supporting Information). The results from these tests show no significant threshold voltage shift under these stress conditions, confirming the long-term operational stability of the Ln-IZO TFT.

The uniformity of the device array is further highlighted by the transfer curves of 150 switch TFTs in the AM-PA (Figure 2e), with typical output characteristics illustrated in Figure 2f. These results confirm the consistent electrical performance of the integrated TFTs, ensuring reliable operation across the sensor array. The distribution of saturation field-effect mobility (μ_{sat}), on/off current ratio, subthreshold slope (SS) determined for one order of magnitude change in I_{DS} , and threshold voltage (V_{th}) extracted for the 150 devices is shown in Figure 2g–j, respectively, demonstrating uniform device performance. The median values for μ_{sat} , SS, and V_{th} were $\approx 8.18 \text{ cm}^2 \text{ V}^{-1} \text{ s}^{-1}$, 0.15 V dec^{-1} , and -1.42 V , respectively. Statistical summaries of these parameters are provided in Table S2 (Supporting Information). To confirm uniform performance across the array, we tested 100 randomly selected 1T-1PD units and observed only minimal variation in their saturation current (Figure S4, Supporting Information). This finding suggests that the additional series resistance introduced by the MoS_2 PD is uniformly distributed, mitigating concerns about pixel-to-pixel variability. Furthermore, we extended both PBS and NBS tests to the TFTs after integrating the MoS_2 PD. The results indicate that threshold voltage shifts under PBS and NBS remain

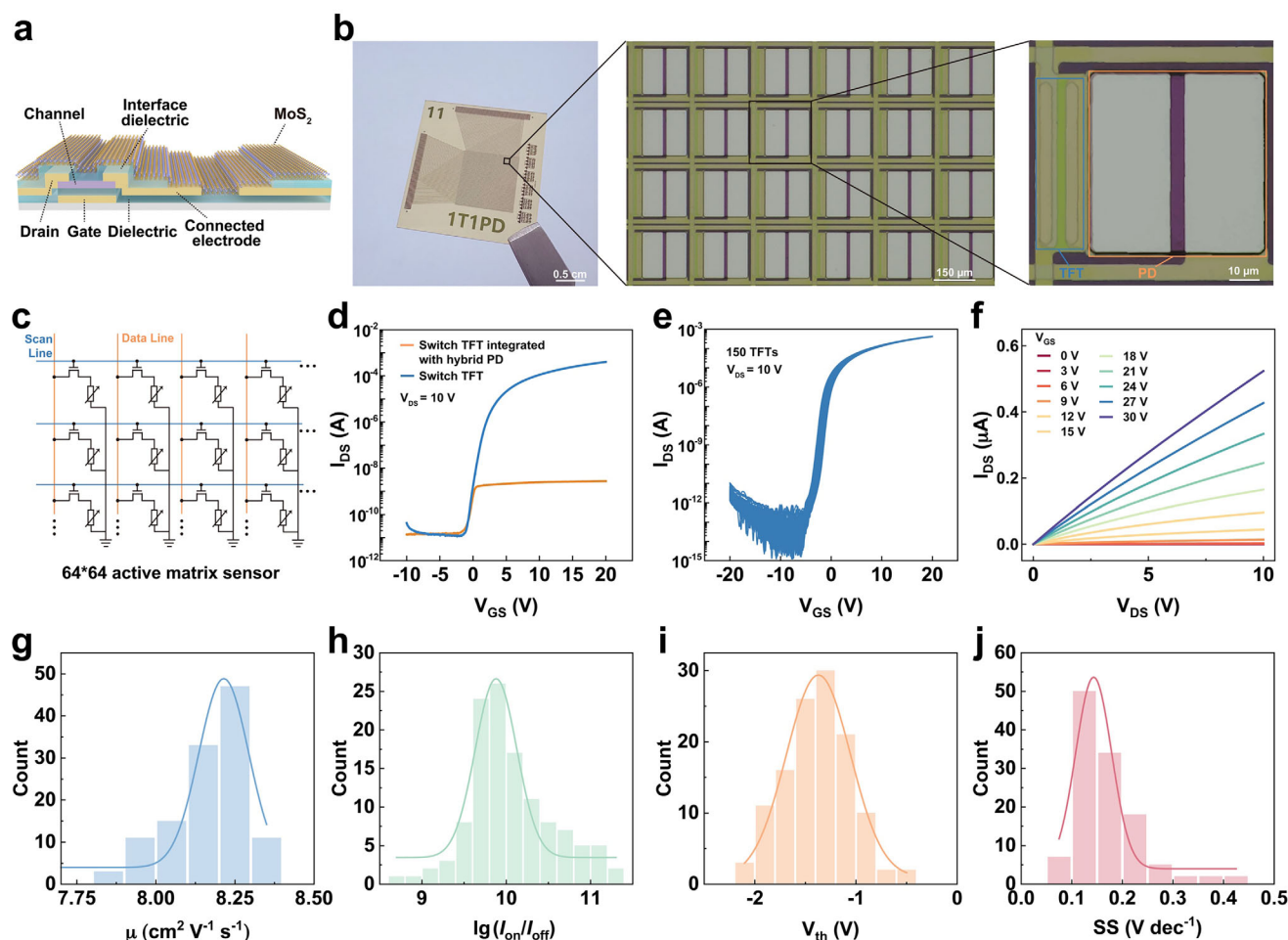


Figure 2. Active-matrix photosensor array (AM-PA). a) Schematic diagram of a single pixel within the AM-PA. b) Optical image of the 64×64 AM-PA. (left panel), with a scale bar of 0.5 cm. The middle panel shows an enlarged segment of the array (scale bar: $150 \mu\text{m}$), and the right panel presents a magnified optical image of a single pixel within the array (scale bar: $10 \mu\text{m}$). c) Equivalent circuit diagram of the AM-PA. d) Transfer curves of the switching thin-film transistor (TFT) and its performance after integration with the hybrid MoS_2 photodetector, sweep range from -10 to 20 V and a smaller step size of 0.05 V. e) Transfer curves for 150 switching TFTs in the AM-PA. f) Typical output curve of the switching Ln-IZO TFT. g–j) Statistical parameters including μ_{sat} , $I_{\text{on}}/I_{\text{off}}$ ratios, V_{th} , and SS for a set of 150 Ln-IZO TFTs.

minimal, demonstrating that the presence of the PD does not cause significant degradation in device performance.

2.3. Light-Tunable Characteristics of MoS_2 PD in AM-PA and Static Image Pre-Processing

Figure 3a illustrates the schematic of MoS_2 PD with a bottom-contact configuration, using monolayer MoS_2 as the photosensitive layer due to its direct bandgap (≈ 1.87 eV), which enhances visible light absorption and photoresponsivity.^[46] The photoluminescence and absorbance Raman spectra of monolayer MoS_2 are shown in Figure S5 (Supporting Information). Furthermore, monolayer MoS_2 can be synthesized over large areas using scalable synthesis techniques, meeting the requirement for optoelectronics and sensing applications that demand uniform and high-quality films for device consistency and performance across wide areas. The MoS_2 PD offers a hardware platform for emulating the photoreceptor functions, leveraging charge-trapping

centers that stem from intrinsic defects in the MoS_2 film.^[47,48] Figure 3b presents the photocurrent generation process in the MoS_2 PD under illumination. The trap centers capture electrons from photogenerated electron-hole pairs, extending carrier lifetime and enhancing photoresponsivity by delaying electron-hole recombination. This effect increases photoconductive gain, enabling high sensitivity even at low light intensities. After removing light, trapped electrons are gradually released, and the gradual release of trapped electrons induces a persistent photocurrent decay, resembling the persistence seen in the human visual system.

We characterized the photoresponse of the monolayer MoS_2 PD across illumination conditions up to $2.0 \mu\text{W cm}^{-2}$ (Figure 3c), showing significant photocurrent enhancement and validating its effectiveness in photon absorption and charge carrier generation. Under optical pulses (0.5 Hz, $0.2 \mu\text{W cm}^{-2}$ at 650 nm), the photocurrent response exhibits a rapidly photo-triggered rise, followed by a slow decay to a new equilibrium after illumination, attributed to charge-trapping centers that inhibit carrier

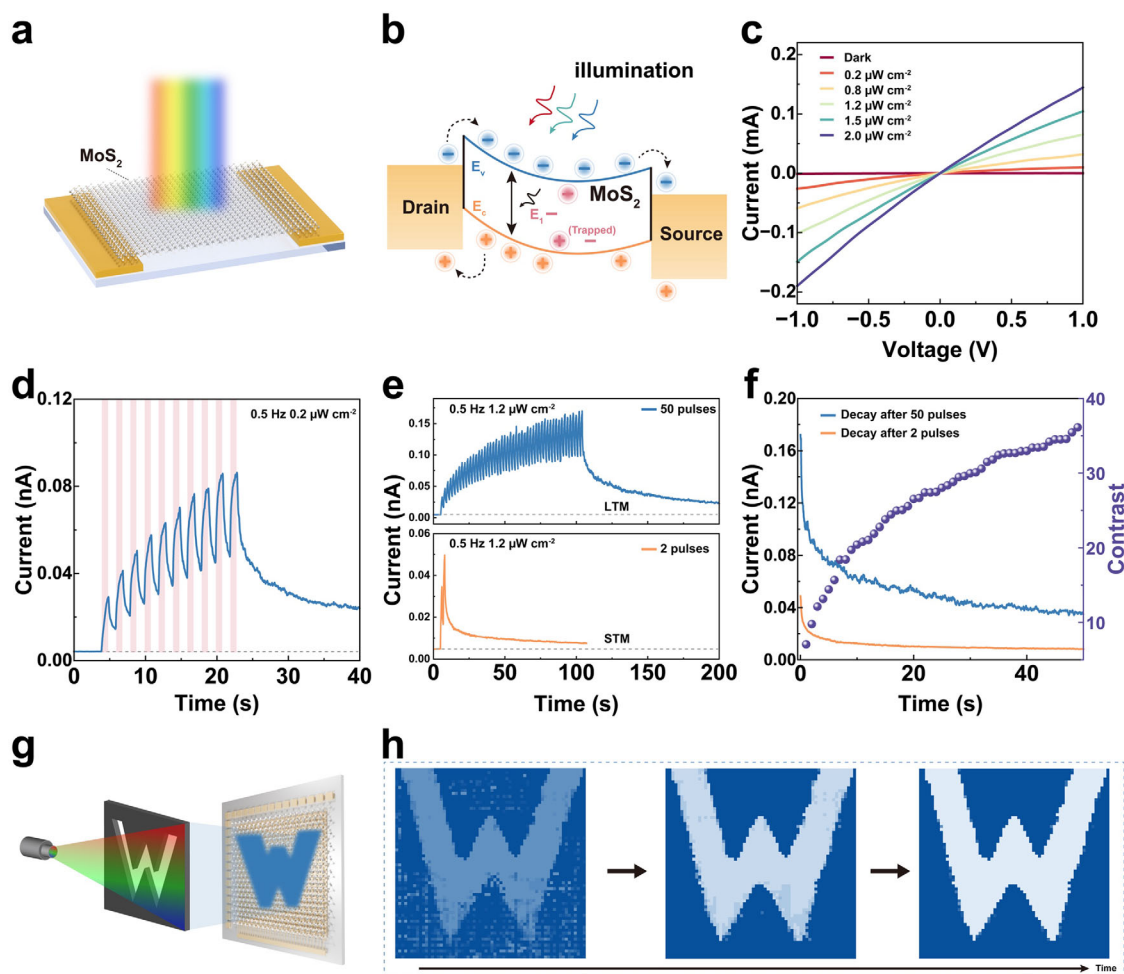


Figure 3. Operation principle of the AM-PA. a) Schematic illustration of the monolayer MoS₂ PD. b) Band diagram of the MoS₂ PD, taking small Schottky barriers at the contacts into consideration. E_F represents the Fermi level energy, E_C is the conduction band minimum, E_V is the valence band maximum, E_I is the localised energy level, and Φ_B denotes the Schottky barrier height. The photocurrent is generated under illumination, with photogenerated electrons or holes becoming trapped in localised states. c) The current-voltage curves on linear scales during a forward sweep (from negative to positive). d) The photocurrent was measured as a function of time under optical pulse stimulation. (650 nm, $0.2 \mu\text{W cm}^{-2}$ at 0.5 Hz, $V_{DS} = 0.1$ V). e) The photocurrent response to 50 optical pulses (top panel) and under two optical pulses (bottom panel). The applied optical pulse was 650 nm with an intensity of $1.2 \mu\text{W cm}^{-2}$ at 0.5 Hz, $V_{DS} = 0.1$ V. f) The photocurrent decay extracted from e), showing the short-term and long-term relaxation processes under 2 and 50 optical pulses, respectively. The contrast between the photocurrent response under 50 optical pulses and in the dark is also shown. g) Schematic diagram of AM-PA for static image sensing. h) Pre-processed image obtained under continued optical pulse stimulations (650 nm, $2.0 \mu\text{W cm}^{-2}$ at 0.5 Hz).

recombination (Figure 3d). Additionally, we evaluated the optoelectronic performance of 100 MoS₂ PDs within the array, extracting key performance features (Figure S6, Supporting Information). All tested devices exhibited high uniformity and configurable conductance plasticity, as illustrated by the individual responses in Figure S7 (Supporting Information). These findings suggest that our approach is both scalable to larger arrays and maintains reliable performance. Moreover, the tunable optoelectronic properties of the MoS₂ PD result in diverse light-modulated conductance plasticity. Short-term memory (STM) is achieved by applying two successive 500 ms optical pulses, resulting in a rapid return of photocurrent close to the initial state. In contrast, long-term memory (LTM) is achieved with 50 successive pulses, where photocurrent is sustained over a longer period (Figure 3e). The extracted decay curves are shown in Figure 3f.

On the other hand, the stored signal can be reset before new data acquisition (Figure S8, Supporting Information).

We then compared the effect of the number of optical pulses, and the extracted decay profiles are well-modeled by a double-exponential function, indicating both fast and slow decay mechanisms corresponding to intrinsic photoconduction and slower trap-related processes, respectively (Figure S9, Supporting Information). In addition, we examined the wavelength-dependent photoconductive response of the MoS₂ PD to further assess its capability to mimic color-sensing functionalities. In human vision, specialized cone cells in the retina respond selectively to specific wavelengths (blue, green, or red), enabling color perception. Similarly, our MoS₂ PD exhibits distinct responsivity to varying wavelengths in the visible range, demonstrating synaptic-like behavior that can be tuned according to each incident wavelength. This

behavior allows the PD to mimic human visual sensitivity for color recognition and lays a foundation for integrating similar devices into artificial vision and color-sensitive optoelectronic systems (Figures S9–S11, Supporting Information). However, unlike the human eye which seamlessly interprets multiple wavelengths of different intensities, our current design demonstrates color selectivity under relatively controlled single-wavelength conditions. To improve multi-wavelength detection fidelity and expand the potential of AM-PA in advanced imaging and real-time color sensing applications, the architecture requires further optimization in future work. For instance, employing optical filtering or refined device stacking could help isolate different spectral components, more closely emulating the multi-cone mechanism of the human retina. Dynamic conductance modulation by varying light pulse frequencies further illustrates the optoelectronic reconfigurability of MoS₂ PD (Figure S12, Supporting Information).

On the other hand, contrast is defined as the average photocurrent ratio between the illuminated target and background pixels (Figure 3f), demonstrating the AM-PA capability in static image pre-processing for improved contrast. Integrating the MoS₂ PD with a TFT array enables contrast enhancement of input images, allowing highlighted key features in complex, noisy backgrounds. For real-time imaging, the AM-PA was connected via wire bonding to an interface PCB board, which was then linked to a source and matrix switch (Figure S13, Supporting Information). Leveraging the light-tunable conductance of the MoS₂ PD, our AM-PA mimics the human visual pre-processing functionality (Figure 3g). Figure 3h provides photocurrent mappings across time scales, where prolonged illumination accentuates grayscale differences between target and background pixels, generating a high-contrast output image that simulates object shape processing along the ventral visual pathway in the human visual system.

2.4. AM-PA for In-Array Visual Spatiotemporal Processing

In addition to enabling static image sensing and pre-processing, the neuromorphic visual sensor array facilitates advanced visual spatiotemporal processing by capturing and analyzing dynamic motion patterns with high temporal resolution. As illustrated in Figure 4a, the human visual system can integrate visual stimuli over time to predict incomplete or evolving inputs. For instance, when a moving light source traces a letter or a trajectory, the brain relies on prior visual cues, such as motion direction and spatial context, to predict the continuation of the movement before the figure is fully formed. This predictive mechanism allows the brain to complete the perception of the letter or trajectory dynamically, enabling rapid and accurate visual interpretation. Such processing is essential for tasks like object tracking and motion analysis.

By mimicking the human visual system's ability to process spatiotemporal information, neuromorphic visual hardware can enhance real-time decision-making in dynamic vision systems. The light-tunable conductance plasticity of the MoS₂ PD in AM-PA offers a unique approach to encoding temporal information sequentially. Notably, the MoS₂ PD shows a delayed recovery of electrical conductivity after light exposure, resulting in residual signals that capture information about the light source's prior

positions. The output current in non-trajectory pixels remained at the dark current level, indicating no light stimulation.

In contrast, trajectory pixels exhibited the expected photocurrent decay behavior due to light exposure. The decay behavior was time-dependent and correlated with the order in which the pixels were exposed to light. Pixels illuminated earlier in the trajectory displayed smaller photocurrent values and longer decay times, reflecting the residual photocurrent characteristic of the device. These time-dependent responses of individual pixels within AM-PA can be exploited to reconstruct the trajectory and direction of a moving light source (Figure 4b, left panel). Such predictions are made by modeling the photoresponse decay characteristics and correlating them with the dynamic illumination pattern of the light source, simulating spatiotemporal visual processing.

As illustrated in the right panel of Figure 4b, when a moving light source writes the letter “U” across the array, the AM-PA predicts the full pattern before the motion is completed. Operationally, the AM-PA captures spatiotemporal input data generated by moving light sources during the experiment, then the input data is processed through a neural network, which applies spatiotemporal information (STI) transformations to predict the future states of the visual field. Details of the STI processing and its mathematical formulation are provided in the Experimental Section. This setup allows for multistep-ahead decision-making, similar to the predictive abilities of the human visual system.

Figure 4c,d illustrates representative detailed results of the AM-PA's motion prediction capabilities. Following the writing process, the pixels of the array are sequentially scanned to retrieve the trajectory, and the written letter “U” can be successfully read out. The data captured by the AM-PA are visualized as grayscale images, while the predicted trajectories are presented in color. The predictions are generated using data from four consecutive columns of the AM-PA array, then the system employs the STI transformation to predict the next two columns in the motion trajectory. The predicted column is integrated with the preceding two columns to iteratively update the input data and generate subsequent movements. By encoding the temporal progression of the light source's motion, the AM-PA accurately tracks the motion of light sources tracing the dynamic pattern of letters “W” and “U.” These results demonstrate the array's ability to integrate and predict dynamic visual inputs, validating its effectiveness in spatiotemporal tracking tasks.

The complete visualization of this process is shown in Figure S14 (Supporting Information). Figure 4e presents five representative motion trajectories, comparing experimentally captured paths with the corresponding predictions made by the AM-PA. The predicted trajectories closely align with the actual recorded data, demonstrating the device's strong capability to process dynamic spatiotemporal inputs and forecast future states, even for complex motion patterns. To quantitatively assess this predictive accuracy, we employed the Structural Similarity Index Measure (SSIM), which evaluates how closely predicted outputs match the experimental results. SSIM scores close to 1 indicate high prediction fidelity. As shown in Figure 4f, the AM-PA consistently achieved SSIM values exceeding 0.75 across various trajectories, indicating high predictive fidelity. These results confirm the array's ability to reliably capture and predict dynamic visual inputs. The AM-PA's ability to process motion data in real time and make quick predictions makes it ideal for applications requiring

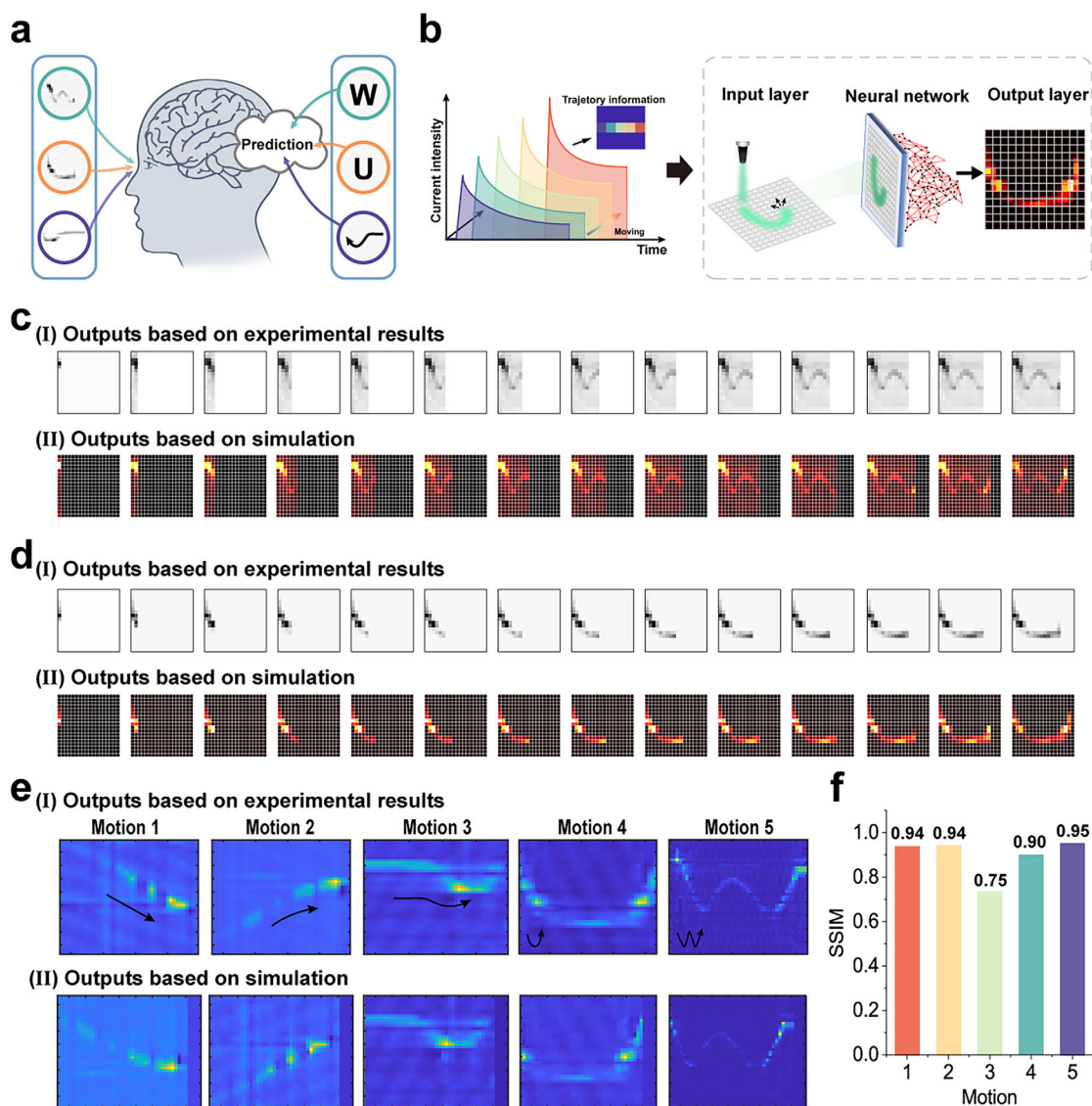


Figure 4. Demonstration of trajectory prediction with AM-PA. a) Schematic of the human visual system integrating temporal visual stimuli to infer incomplete or evolving motion inputs. b) Illustration of light-tunable conductance plasticity enabling in-sensor trajectory information processing (left panel) and artificial neural network-assisted AM-PA for trajectory prediction (right panel). c,d) Detailed comparison of experimental and simulated predictive outputs for two representative motion patterns. (I) Experimental outputs: AM-PA captures the trajectory information of a moving light source. (II) Simulated predictive outputs: using the first four experimentally acquired frames from (I), the subsequent two frames are predicted, reconstructing the complete trajectory from partial data. e) Comparison of experimental (I) and simulated (II) outputs for five different motions using AM-PA. f) Structure similarity index measure (SSIM) evaluation of the simulated predictions against the corresponding experimental results in (e).

accuracy and fast decision-making, highlighting its potential in advanced optoelectronic systems.

We further investigated the spatiotemporal integration capabilities of the AM-PA system by processing real motion scenes. High accuracy and rapid motion prediction are essential for machine vision applications, such as autonomous vehicles and surveillance, where delayed perception can compromise safety. To address this, we focused on decision-critical elements for autonomous driving, including traffic lights, nearby vehicles, and lane markings (Figure 5a). To evaluate the proposed neuromorphic visual system based on AM-PA, we designed experiments that simulate motion prediction under real-world conditions. The

AM-PA captured visual information, enabling us to assess its ability to track and predict motion effectively. The sampled motion frames were collected at 0.5 s intervals across various unstructured driving scenarios to replicate the complexity of autonomous environments. These scenarios included pedestrian prediction during road crossing (Scene 1), a nearby pedestrian crossing (Scene 2), and abrupt changes in vehicle orientation (Scene 3), as illustrated in Figure 5b.

Leveraging its dynamic light-modulated capability under visible light, the AM-PA converts external motion data into image patterns for spatiotemporal processing. The captured image frames, spanning different time intervals, depict trajectory routes

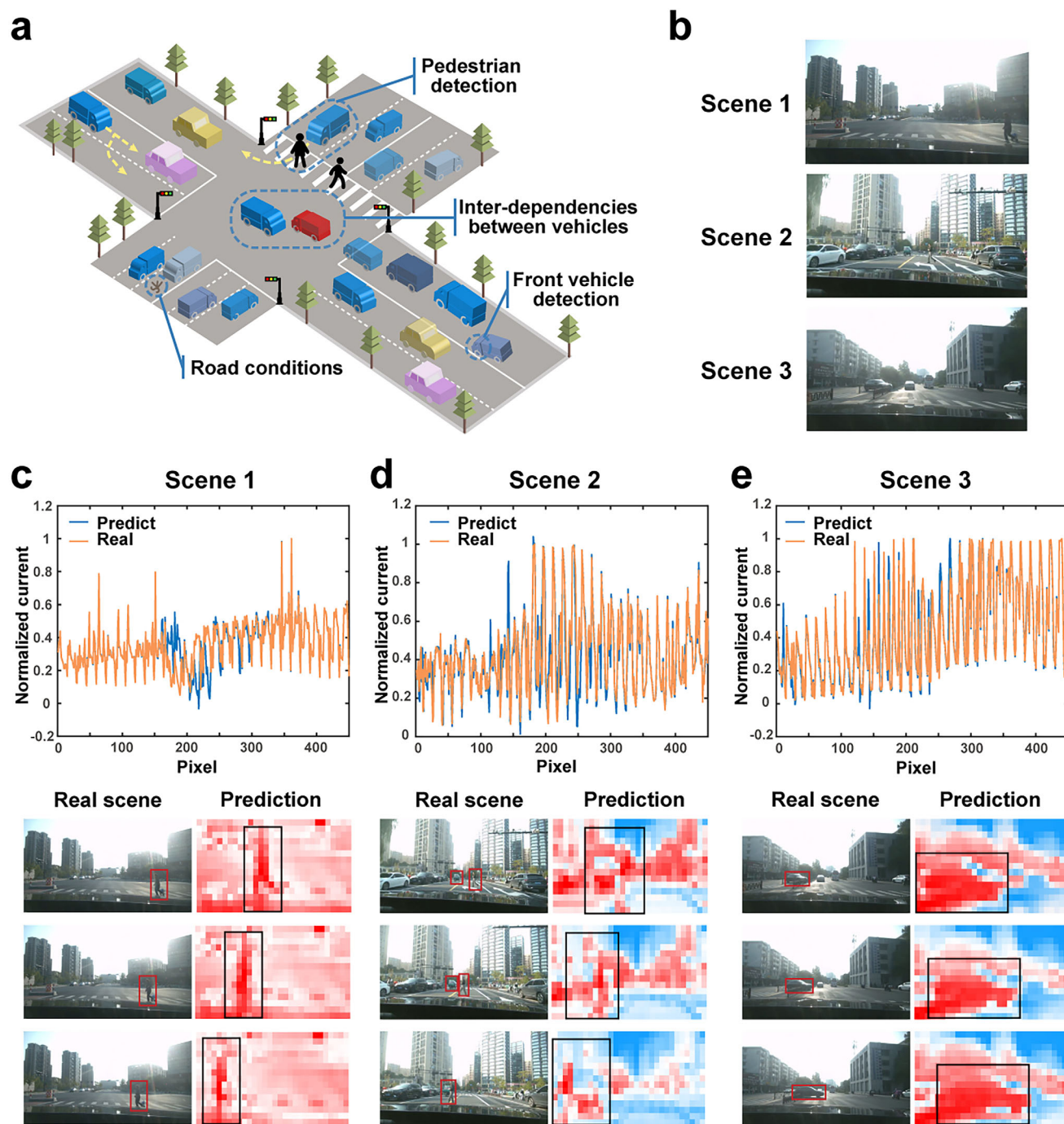


Figure 5. Generalisation capability of visual processing in unstructured environments. a) Schematic diagram of applicable scenarios based on the AM-PA vision array in real scenes, including road conditions, pedestrian, and vehicle detection. b) Corresponding real-world scenes of the example visual processing. c-e) Comparison between captured real-scene trajectories and simulated predictive outputs for three distinct motion scenarios. Sequential image frames recorded over time (from t_0 to t_{end}) are used to extract motion trajectories. The first few frames are employed to predict subsequent frames, and the predicted results are compared with actual scene data to evaluate accuracy.

from t_0 to t_{end} (Figure S15, Supporting Information). To simulate real-life motion detection, specific frames were extracted and analyzed. By collecting motion information over a 4 s window, the AM-PA applies STI transformation to accurately predict motion states 2.5 s ahead. The neuromorphic visual system produced

compressive temporal frames that encode trajectory contours, facilitating motion recognition and location tracking.

Unlike conventional image sensors, which only capture present stimuli, the AM-PA's compressive imaging preserves the relative spatial positions of objects, enabling more effective

in-array analysis of dynamic scenes. Figure 5c–e illustrates the prediction results for three distinct scenarios, where the system achieved prediction accuracies of 85%, 87%, and 92%, respectively, after 2.5 s. The entire prediction process is detailed in Figure S16 (Supporting Information), while Figure S17 (Supporting Information) shows a comparison between real motion scenes and their corresponding predicted trajectories. The STI equation solution is computed in just 8 milliseconds, enabling near-real-time predictions. These results demonstrate the AM-PA system's robust ability to predict the movement intentions of pedestrians and vehicles with high accuracy, validating its effectiveness for spatiotemporal tracking. This capability underscores the system's potential for enhancing autonomous driving technologies by providing reliable and timely motion predictions essential for safety and decision-making.

3. Conclusion

In summary, we have developed a 64×64 active-matrix photosensor array (AM-PA) integrating lanthanide-doped indium zinc oxide (Ln-IZO) thin-film transistors and monolayer MoS_2 photodetectors. Intrinsic defects in the MoS_2 layer create charge-trapping centers that enable light information storage and dynamic modulation of optoelectronic properties. Leveraging light-tunable conductance, the AM-PA shows capabilities consistent with neuromorphic visual processing, including effective static image sensing and noise reduction through in-sensor pre-processing. Furthermore, the AM-PA demonstrated high image fidelity with a Structural Similarity Index Measure (SSIM) of 0.95 when predicting dynamic visual inputs. Additionally, it achieved advanced visual spatiotemporal processing by accurately forecasting complex motion trajectories with an accuracy of 92%. These high-performance metrics underscore the AM-PA's efficiency in managing and interpreting complex visual information, highlighting its significant potential for advanced neuromorphic visual hardware.

4. Experimental Section

Device Array Fabrication: The metal-oxide thin-film transistor array was home-designed and taped out at Guangzhou Newvision Opto. Tech. Co. Ltd. Briefly, a 200 nm-thick molybdenum (Mo) layer, serving as the gate electrode, was deposited onto glass substrates via direct-current (DC) sputtering and patterned through wet etching. A gate insulator comprising 250 nm Si_3N_4 and 50 nm SiO_2 stack was then deposited using plasma-enhanced chemical vapor deposition (PECVD). Next, a 30 nm-thick active layer of lanthanide-doped indium zinc oxide (Ln-IZO) was deposited via radio-frequency (RF) magnetron co-sputtering using an IZO (In/Zn, 1:1) ceramic target. The films were annealed at 350 °C in the air for 30 min and patterned through oxalic acid wet etching. Source and drain electrodes were formed by depositing a 200 nm-thick Mo layer via DC sputtering, followed by wet etching. The channel dimensions were set with a width-to-length ratio (W/L) of 105 $\mu\text{m}/5 \mu\text{m}$. A 200 nm-thick SiO_2 passivation layer was deposited via PECVD. This layer also serves as an interface dielectric and was selectively patterned to expose the electrode areas. All thin-film transistors (TFTs) underwent a final annealing step at 350 °C in air for 30 min.

The monolayer MoS_2 was transferred using a conventional wet transfer technique. The MoS_2 layer was spin-coated twice with 950K A4 poly(methyl methacrylate) (PMMA) resist, each time baked at 180 °C for 90 s. After transferring to the substrate via deionized (DI) water, the device under-

went sequential annealing at 80 °C for 30 min, 120 °C for 1 h, and 150 °C for 1 h to remove residual moisture between the MoS_2 layer and the substrate. To remove the PMMA layer, the device was immersed in hot acetone (50 °C) for 10 min, followed by rinsing with isopropanol to ensure a clean surface. As a result, when the MoS_2 layer was transferred onto the array, it only formed electrical contact at the exposed electrode regions, naturally defining the active areas without requiring further MoS_2 patterning.

Material Characterization: Photoluminescence (PL) spectra were obtained using a WITec Alpha 300R Raman spectrometer with 532 nm laser excitation (1 mW power). Diffraction gratings of 3000 and 300 g mm^{-1} were used for PL measurements to optimize spectral range and resolution. Absorbance spectrum was recorded using a UV-Vis-NIR microspectrophotometer (CRAIC 20/30V, CRAIC Technologies).

Electrical Characterization: Electrical measurements (transfer curves and output curves) were performed under ambient conditions at room temperature using a Keithley 4200 SCS semiconductor parameter analyzer. The optoelectronic response to varying optical signals was assessed with a Tektronix AFG3152C arbitrary function generator triggering an LED, while current measurements were recorded using a Keysight B1500 parameter analyzer. For the AM-PA, characterization was performed using peripheral component interconnect (PCI) extensions for instrumentation (PXI, National Instruments) system with a LabVIEW-based custom-made program. The PXI system was comprised of an NI PXIe-1073 PXI chassis equipped with an NI PXIe-2531 matrix switch module and NI PXIe-4138 source measure units for data acquisition. Control, processing, and readout operations were automated via LabVIEW software. The photosensor array's source, drain, and gate terminals were wire-bonded to a custom 129-lead PCB, interfacing directly with the matrix switch and source through connecting cables. The optical stimuli were generated by a 450/520/650 nm semiconductor laser (Changchun New Industries Optoelectronics Tech Co., Ltd, China). The light intensity was measured using a standard silicon photodiode (S120VC, Thorlabs). The TFT parameters were extracted as follows:

$$SS = \frac{\partial V_{GS}}{\partial (\lg I_{DS})} \quad (1)$$

$$\mu_{\text{sat}} = \frac{2L}{WC_{\text{ox}}} \left(\frac{\partial \sqrt{I_{DS}}}{\partial V_{GS}} \right)^2 \quad (2)$$

Spatio-temporal information (STI) Transformation: This transformation facilitates the conversion of spatial information from high-dimensional data into temporal information for any target variable. The STI equations were formulated as Equation (3) at time $t = 1, 2, \dots, m$.

$$\begin{cases} \Phi(X^t) = Y^t \\ X^t = \Psi(Y^t) \end{cases} \quad (3)$$

where Φ and Ψ were the differentiable functions from $R^D \rightarrow R^L$ and $R^L \rightarrow R^D$, respectively. These functions were such that $\Phi \circ \Psi = \text{id}$, where “ \circ ” denotes function composition, and “id” represents the identity function. Specifically, X^t denotes the spatial information at time t , with dimension D , and Y^t denoting the future temporal information of any variable in X^t with dimension L . Function Φ encodes the spatial information X^t into time information Y^t and function Ψ restores the encoded time information Y^t to the original spatial information X^t . Several techniques, exist for solving the conjugated Equation (3), including the Levenberg–Marquardt method.^[49]

Statistical Analysis: All the electrical data were processed in Origin (OriginPro 2021, OriginProLab).

Supporting Information

Supporting Information is available from the Wiley Online Library or from the author.

Acknowledgements

Y.C. and R.W. contributed equally to this work. This work was supported by the National Natural Science Foundation of China (Grant Nos. 62174138, and 92464105), the Key Project of Westlake Institute for Optoelectronics (No. 2023GD004), and the Research Center for Industries of the Future (RCIF) at Westlake University (No. WU2023C008). The authors thank the Westlake Centre for Micro/Nano Fabrication, the Instrumentation and Service Centre for Physical Sciences (ISCPS), and the Instrumentation and Service Centre for Molecular Sciences (ISCMS) at Westlake University for the facility support and technical assistance.

Conflict of Interest

The authors declare no conflict of interest.

Data Availability Statement

The data that support the findings of this study are available from the corresponding author upon reasonable request.

Keywords

2D materials, active-matrix array, neuromorphic vision, visual processing

Received: March 29, 2025
Published online:

- [1] F. Aguirre, A. Sebastian, M. L. e Gallo, W. Song, T. Wang, J. J. Yang, W. Lu, M.-F. Chang, D. Ielmini, Y. Yang, A. Mehnich, A. Kenyon, M. A. Villena, J. B. Roldán, Y. Wu, H.-H. Hsu, N. Raghavan, J. Suñé, E. Miranda, A. Eltawil, G. Setti, K. Smagulova, K. N. Salama, O. Krestinskaya, X. Yan, K.-W. Ang, S. Jain, S. Li, O. Alharbi, S. Pazos, et al., *Nat. Commun.* **2024**, *15*, 1974.
- [2] A. Sebastian, M. L. e Gallo, R. Khaddam-Aljameh, E. Eleftheriou, *Nat. Nanotechnol.* **2020**, *15*, 529.
- [3] R. Fontaine, in Proc. Int. Image Sensors Workshop (IISW), International Image Sensor Society (IISS), Vaals, the Netherlands, **2015**, pp. 6.
- [4] Q. Chen, X. Hu, L. Wen, Y. Yu, D. R. Cumming, *Small* **2016**, *12*, 4922.
- [5] N. Dean, *Nat. Nanotechnol.* **2015**, *10*, 15.
- [6] M. Bigas, E. Cabruja, J. Forest, J. Salvi, *Microelectron. J.* **2006**, *37*, 433.
- [7] F. Zhou, Y. Chai, *Nat. Electron.* **2020**, *3*, 664.
- [8] T. Wan, B. Shao, S. Ma, Y. Zhou, Q. Li, Y. Chai, *Adv. Mater.* **2022**, *34*, 2203830.
- [9] S. Zhu, T. Xie, Z. Lv, Y. B. Leng, Y. Q. Zhang, R. Xu, J. Qin, Y. Zhou, V. A. L. Roy, S. T. Han, *Adv. Mater.* **2023**, *35*, 2301986.
- [10] C. Choi, G. J. Lee, S. Chang, Y. M. Song, D. H. Kim, *Adv. Mater.* **2024**, *36*, 2412252.
- [11] Q. Ren, C. Zhu, S. Ma, Z. Wang, J. Yan, T. Wan, W. Yan, Y. Chai, *Adv. Mater.* **2024**, *36*, 2407476.
- [12] Y. Chen, M. Nazhamaiti, H. Xu, Y. Meng, T. Zhou, G. Li, J. Fan, Q. Wei, J. Wu, F. Qiao, L. Fang, Q. Dai, *Nature* **2023**, *623*, 48.
- [13] T. Baden, T. Euler, P. Berens, *Nat. Rev. Neurosci.* **2020**, *21*, 5.
- [14] Z. Long, Y. Zhou, Y. Ding, X. Qiu, S. Poddar, Z. Fan, *Nat. Rev. Mater.* **2024**, *10*, 128.
- [15] Z. Wang, T. Wan, S. Ma, Y. Chai, *Nat. Nanotechnol.* **2024**, *19*, 919.
- [16] H. Huang, X. Liang, Y. Wang, J. Tang, Y. Li, Y. Du, W. Sun, J. Zhang, P. Yao, X. Mou, F. Xu, J. Zhang, Y. Lu, Z. Liu, J. Wang, Z. Jiang, R. Hu, Z. Wang, Q. Zhang, B. Gao, X. Bai, L. Fang, Q. Dai, H. Yin, H. Qian, H. Wu, *Nat. Nanotechnol.* **2024**, *20*, 93.
- [17] B. Dang, T. Zhang, X. Wu, K. Liu, R. Huang, Y. Yang, *Nat. Electron.* **2024**, *7*, 991.
- [18] C. Jin, J. Wang, S. Yang, Y. Ding, J. Chang, W. Liu, Y. Xu, X. Shi, P. Xie, J. C. Ho, C. Wan, Z. Zheng, J. Sun, L. Liao, J. Yang, *Adv. Mater.* **2024**, *36*, 2410398.
- [19] S. Duan, X. Zhang, Y. Xi, D. Liu, X. Zhang, C. Li, L. Jiang, L. Li, H. Chen, X. Ren, W. Hu, *Adv. Mater.* **2024**, *36*, 2405030.
- [20] Y. Zheng, S. Ghosh, S. Das, *Adv. Mater.* **2023**, *36*, 2307380.
- [21] D. Li, Y. Chen, H. Ren, Y. Tang, S. Zhang, Y. Wang, L. Xing, Q. Huang, L. Meng, B. Zhu, *Adv. Sci.* **2024**, *11*, 2406401.
- [22] D. Li, Z. Jia, Y. Tang, C. Song, K. Liang, H. Ren, F. Li, Y. Chen, Y. Wang, X. Lu, L. Meng, B. Zhu, *Nano Lett.* **2022**, *22*, 5434.
- [23] M. Dong, Y. Zhang, J. Zhu, X. Zhu, J. Zhao, Q. Zhao, L. Sun, Y. Sun, F. Yang, W. Hu, *Adv. Mater.* **2024**, *36*, 2409550.
- [24] G. Gong, Y. Zhou, Z. Xiong, T. Sun, H. Li, Q. Li, W. Zhao, G. Zhang, Y. Zhai, Z. Lv, H. Tan, Y. Zhou, S. T. Han, *Adv. Mater.* **2024**, *36*, 2409844.
- [25] S. Ma, Y. Zhou, T. Wan, Q. Ren, J. Yan, L. Fan, H. Yuan, M. Chan, Y. Chai, *Nano Lett.* **2024**, *24*, 7091.
- [26] M. Deng, Z. Li, S. Liu, X. Fang, L. Wu, *Nat. Commun.* **2024**, *15*, 8789.
- [27] F. Cao, Z. Hu, T. Yan, E. Hong, X. Deng, L. Wu, X. Fang, *Adv. Mater.* **2023**, *35*, 2304550.
- [28] C. Choi, G. J. Lee, S. Chang, Y. M. Song, D.-H. Kim, *ACS Nano* **2024**, *18*, 1241.
- [29] P. S. Wu, T. He, H. Zhu, Y. Wang, Q. Li, Z. Wang, X. Fu, F. Wang, P. Wang, C. X. Shan, Z. Y. Fan, L. Liao, P. Zhou, W. D. Hu, *Infomat* **2022**, *4*, 12275.
- [30] N. Li, S. Zhang, Y. Peng, X. Li, Y. Zhang, C. He, G. Zhang, *Adv. Funct. Mater.* **2023**, *33*, 2305589.
- [31] J. Bai, D. He, B. Dang, K. Liu, Z. Yang, J. Wang, X. Zhang, Y. Wang, Y. Tao, Y. Yang, *Adv. Mater.* **2024**, *36*, 2401060.
- [32] Y. Zhou, J. Fu, Z. Chen, F. Zhuge, Y. Wang, J. Yan, S. Ma, L. Xu, H. Yuan, M. Chan, X. Miao, Y. He, Y. Chai, *Nat. Electron.* **2023**, *6*, 870.
- [33] S. Subbulakshmi Radhakrishnan, A. Dodda, S. Das, *ACS Nano* **2022**, *16*, 20100.
- [34] D. Jayachandran, A. Pannone, M. Das, T. F. Schranghamer, D. Sen, S. Das, *ACS Nano* **2022**, *17*, 1068.
- [35] S. Lee, R. Peng, C. Wu, M. Li, *Nat. Commun.* **2022**, *13*, 1485.
- [36] F. Liao, Z. Zhou, B. J. Kim, J. Chen, J. Wang, T. Wan, Y. Zhou, A. T. Hoang, C. Wang, J. Kang, J.-H. Ahn, Y. Chai, *Nat. Electron* **2022**, *5*, 84.
- [37] P. Y. Huang, B. Y. Jiang, H. J. Chen, J. Y. Xu, K. Wang, C. Y. Zhu, X. Y. Hu, D. Li, L. Zhen, F. C. Zhou, J. K. Qin, C. Y. Xu, *Nat. Commun.* **2023**, *14*, 6736.
- [38] H. Jang, C. Liu, H. Hinton, M. H. Lee, H. Kim, M. Seol, H. J. Shin, S. Park, D. Ham, *Adv. Mater.* **2020**, *32*, 2002431.
- [39] J. Chen, Z. Zhou, B. J. Kim, Y. Zhou, Z. Wang, T. Wan, J. Yan, J. Kang, J. H. Ahn, Y. Chai, *Nat. Nanotechnol.* **2023**, *18*, 882.
- [40] Y. Gong, P. Xie, X. Xing, Z. Lv, T. Xie, S. Zhu, H. H. Hsu, Y. Zhou, S. T. Han, *Adv. Funct. Mater.* **2023**, *33*, 2303539.
- [41] A. Dodda, D. Jayachandran, A. Pannone, N. Trainor, S. P. Stepanoff, M. A. Steves, S. S. Radhakrishnan, S. Bachu, C. W. Ordenez, J. R. Shallenberger, J. M. Redwing, K. L. Knappenberger, D. E. Wolfe, S. Das, *Nat. Mater.* **2022**, *21*, 1379.
- [42] A. Dodda, D. Jayachandran, S. Subbulakshmi Radhakrishnan, A. Pannone, Y. Zhang, N. Trainor, J. M. Redwing, S. Das, *ACS Nano* **2022**, *16*, 20010.
- [43] D. Jayachandran, A. Oberoi, A. Sebastian, T. H. Choudhury, B. Shankar, J. M. Redwing, S. Das, *Nat. Electron.* **2020**, *3*, 646.

- [44] S. E. Ahn, I. Song, S. Jeon, Y. W. Jeon, Y. Kim, C. Kim, B. Ryu, J. H. Lee, A. Nathan, S. Lee, G. T. Kim, U. I. Chung, *Adv. Mater.* **2012**, *24*, 2631.
- [45] B. Bao, D. D. Karnaushenko, O. G. Schmidt, Y. Song, D. Karnaushenko, *Adv. Intell. Syst.* **2022**, *4*, 2100253.
- [46] Y. C. Lin, R. Torsi, R. Younas, C. L. Hinkle, A. F. Rigosi, H. M. Hill, K. Zhang, S. Huang, C. E. Shuck, C. Chen, Y. H. Lin, D. Maldonado-Lopez, J. L. Mendoza-Cortes, J. Ferrier, S. Kar, N. Nayir, S. Rajabpour, A. C. T. van Duin, X. Liu, D. Jariwala, J. Jiang, J. Shi, W. Mortelmans, R. Jaramillo, J. M. J. Lopes, R. Engel-Herbert, A. Trofe, T. Ignatova, S. H. Lee, Z. Mao, et al., *ACS Nano* **2023**, *17*, 9694.
- [47] H. Qiu, T. Xu, Z. Wang, W. Ren, H. Nan, Z. Ni, Q. Chen, S. Yuan, F. Miao, F. Song, G. Long, Y. Shi, L. Sun, J. Wang, X. Wang, *Nat. Commun.* **2013**, *4*, 2642.
- [48] M. M. Furchi, D. K. Polyushkin, A. Pospischil, T. Mueller, *Nano Lett.* **2014**, *14*, 6165.
- [49] C. Kanzow, N. Yamashita, M. Fukushima, *J. Comput. Appl. Math.* **2005**, *173*, 321.